

Article

Effect of Centrifugal Force on Power Output of a Spin-Coated Poly(Vinylidene Fluoride-Trifluoroethylene)-Based Piezoelectric Nanogenerator

Dong Geun Jeong, Huidrom Hemojit Singh, Mi Suk Kim and Jong Hoon Jung * 

Department of Physics, Inha University, Incheon 22212, Republic of Korea

* Correspondence: jhjung@inha.ac.kr; Tel.: +82-32-860-7659

Abstract: While poly(vinylidene fluoride-trifluoroethylene) (P(VDF-TrFE)) film is an excellent piezoelectric material for mechanical energy harvesting, the piezoelectric output varies considerably with the spin coating conditions. Herein, we reported a systematic evaluation of the structural, electrical, mechanical, and microstructural properties of spin-coated P(VDF-TrFE) films obtained at various distances from the center, as well as under different rotational speeds. With increasing distance, the remnant polarization, dielectric constant, and crystallinity of the films increased, which resulted in enhanced piezoelectric power at the largest distance. With increasing rotational speed, the remnant polarization, dielectric constant, and crystallinity of the films initially increased and then decreased, while the Young's modulus continuously increased. This resulted in an enhanced piezoelectric power at a given rotational speed. The piezoelectric power is proportional to the remnant polarization and inversely proportional to the Young's modulus. The highest (2.1 mW) and lowest (0.5 mW) instantaneous powers were obtained at the largest ($1.09 \mu\text{C}/\text{cm}^2 \cdot \text{GPa}^{-1}$) and smallest ($0.60 \mu\text{C}/\text{cm}^2 \cdot \text{GPa}^{-1}$) value of remnant polarization over Young's modulus, respectively. We explain these behaviors in terms of the centrifugal force-induced shear stress and grain alignment, as well as the thickness-dependent β -phase crystallization and confinement. This work implies that the spin coating conditions of distance and rotational speed should be optimized for the enhanced power output of spin-coated P(VDF-TrFE)-based piezoelectric nanogenerators.

Keywords: spin-coated P(VDF-TrFE); shear stress; grain alignment; crystallization; confinement; power output; piezoelectric nanogenerator



Citation: Jeong, D.G.; Singh, H.H.; Kim, M.S.; Jung, J.H. Effect of Centrifugal Force on Power Output of a Spin-Coated Poly(Vinylidene Fluoride-Trifluoroethylene)-Based Piezoelectric Nanogenerator. *Energies* **2023**, *16*, 1892. <https://doi.org/10.3390/en16041892>

Academic Editors: Wael A. Altabay and Sallam A. Kouritem

Received: 20 January 2023

Revised: 9 February 2023

Accepted: 13 February 2023

Published: 14 February 2023



Copyright: © 2023 by the authors. Licensee MDPI, Basel, Switzerland. This article is an open access article distributed under the terms and conditions of the Creative Commons Attribution (CC BY) license (<https://creativecommons.org/licenses/by/4.0/>).

1. Introduction

The rapid depletion of fossil fuels and climate change problems have prompted great interest in energy harvesting from the environment. In particular, wasted mechanical energy harvesting in our daily life has been considered as one of the most promising techniques to power small electronic devices and various sensors without traditional batteries in the forthcoming Internet of Things (IoT) era [1,2]. In contrast to solar and thermal energies, mechanical vibrations are abundant and ubiquitous aspects of human motion, wind, and ocean waves and are less susceptible to environmental factors, such as time and geographic location [3]. Notably, low-frequency mechanical energies have been effectively converted to electricity using a recently developed piezoelectric nanogenerator (PENG) [4–8]. One of the key factors in increasing the mechanical energy harvesting efficiency in PENGs is choosing appropriate materials [9,10] and inventing innovative device structures [11,12].

Among the various piezoelectric materials, poly(vinylidene fluoride-trifluoroethylene) (P(VDF-TrFE)) is one of the most plausible candidates for highly efficient PENG applications, due to its high remnant polarization, high piezoelectric coefficient, flexibility, and chemical stability [13–16]. Especially, its solution processability allows P(VDF-TrFE) to be used in cost-effective and large-area mechanical energy harvesting applications. The facile

spin coating technique is being widely used for the fabrication of the P(VDF-TrFE) films. However, spin-coated P(VDF-TrFE) films exhibit significant variation in their physical properties, even for the same VDF:TrFE content, solvent, rotational speed, and duration time [17–20]. Therefore, it is essential to understand the origin of these variances during spin coating to ensure the fabrication of reliable and stable P(VDF-TrFE)-based PENGs.

In this paper, we report the structural, electrical, mechanical, and microstructural properties of P(VDF-TrFE) film specimens fabricated at various distances from the center, as well as under different rotational speeds, during the conventional spin coating. While all P(VDF-TrFE) film specimens exhibited ferroelectricity and piezoelectricity, we found that the local crystalline phase, crystallinity, grain orientation, and grain density significantly varied, depending on the spin coating conditions. Such variations were significant for rotational speed, rather than the distance from the center. A systematic investigation showed that centrifugal force-induced shear force, as well as thickness-dependent β -phase crystallization and confinement, were responsible for the observed variable remnant polarization, dielectric constant, Young's modulus, and hence, piezoelectric power output. Enhanced remnant polarization and reduced Young's modulus through the optimized spin coating condition would be essential for the highly efficient P(VDF-TrFE)-based piezoelectric nanogenerators.

2. Materials and Methods

2.1. Fabrication

P(VDF-TrFE) films, with a composition of VDF:TrFE = 70:30 mol%, were fabricated using a conventional spin coating method. The films were chosen for their highest ferroelectric responses of polarization and switching rate among various compositions [21]. Commercially available P(VDF-TrFE) powder with high purity (PolyK Technologies) was dissolved in N, N-dimethylformamide (DMF) solvent (10 wt%, purity > 99.8%, Sigma Aldrich), and the solution was continuously stirred for 24 h. The solution was then poured onto a Pt-coated SiO₂/Si substrate (200 $\mu\text{m} \pm 1.5$ nm, Quintess Co., Ltd., Incheon, Republic of Korea), and the spin coating was performed at various rotational speeds for 30 sec under ambient conditions. The films were put in a furnace (AJ-SB4, Ajeon Co., Namyangju, Republic of Korea) for pyrolysis, in which the furnace was maintained at 80 °C for 30 min and further annealed at 140 °C for 2 h. Pyrolysis is performed to evaporate the solvent, while annealing is performed to crystallize the films.

2.2. Characterization

The crystalline structure and phase purity of the P(VDF-TrFE) films were characterized using high-resolution X-ray diffraction (X'PERT-PRO, PANalytical) with Cu K α radiation. The chemical bonding vibrations of P(VDF-TrFE) were examined using Fourier transform-infrared (FT-IR) spectroscopy with attenuated total internal reflection (ATR) (VERTEX 80 V, Bruker). For the ATR measurements, small pieces of P(VDF-TrFE) film (0.5 \times 1 cm²) were cut using a diamond cutter and attached to a ZnSe crystal, providing multiple reflections of infrared light. The surface and cross-section morphologies were investigated by atomic force microscopy (NX10, PSIA) and field emission scanning electron microscopy (S-4300SE, HITACHI), respectively. The ferroelectric hysteresis loop and complex dielectric constant were obtained using a ferroelectric tester (Precision Multiferroic Tester, Radiant Technologies, Inc., Albuquerque, NM, USA) and an LCR meter (4284A, Hewlett-Packard, Palo Alto, CA, USA), respectively. For the electrical measurements, Au (500 \pm 50 Å) was deposited as a top electrode using a sputter coater (Sputter coater 108, Cressington, Watford, UK). The crystallinity of the films was investigated by differential scanning calorimetry (404F1, NETZSCH, Selb, Germany). For the differential scanning calorimetry (DSC) measurements, the films were heated to 180 °C at a rate of 5 °C/min under the flowing Ar gas. The Young's modulus was determined using a nanoindenter (G200, KLA instrument, Chandler, AZ, USA) and a custom-made indenter (Namil Optical Instruments, Incheon, Republic of Korea).

2.3. Piezoelectric Power Generation Measurement

We deposited a thin poly(methyl methacrylate) (PMMA) layer (100 ± 10 nm, MicroChem) on the P(VDF-TrFE) film to form a passivation layer [22] and then sputtered Au to form an electrode in the PENG. Two Cu wires were attached to the Au top electrode and Pt bottom electrode. The piezoelectric outputs of the P(VDF-TrFE)-based PENG were characterized using a custom-made linear motor system (LM-NK237603, Motorbank, Seoul, Republic of Korea) to periodically apply and release a force (10 N) at a frequency of 1 Hz. Electrical outputs were measured using a two-channel digital phosphor oscilloscope (DSOX2002A, Keysight, Santa Rosa, CA, USA), a programmable electrometer (6517, Keithley), and a low-noise current preamplifier (SR570, Stanford Research Systems, Sunnyvale, CA, USA). To minimize noise, all electrical measurements were conducted inside a Faraday cage.

3. Results and Discussion

The distance (r) from the center and rotational speed (ω) were varied during spin coating to systematically investigate the effect of centrifugal force on the physical properties of the P(VDF-TrFE) films. As shown in Figure 1a, the P(VDF-TrFE) film specimens with dimensions of 1×1 cm² were obtained at distances of $r = 0, 2,$ and 4 cm, and at rotational speeds of $\omega = 1000, 3000,$ and 7000 rpm. Note that the amount of P(VDF-TrFE) solution for the spin coating was kept constant at 10 mL.

Figure 1b shows cross-sectional scanning electron microscopy (SEM) images of the P(VDF-TrFE) films. The P(VDF-TrFE) films were uniform and dense, without noticeable voids. The thickness of the films appears to be more influenced by the rotational speed, rather than the distance. Quantitative estimations of the film thickness show that, for films obtained at rotational speeds of 1000, 3000, and 7000 rpm, the estimated thicknesses are 1080, 640, and 360 nm, respectively. For films obtained at distances of 0–4 cm from the center, the estimated thickness is between 620 and 640 nm. This behavior can be attributed to the fact that centrifugal force primarily depends on rotational speed, rather than distance [23].

In Figure 1c, we show X-ray diffraction patterns of P(VDF-TrFE) film specimens for a diffraction angle of $2\theta = 16\text{--}24^\circ$. Irrespective of distance and rotational speed, a single diffraction peak was observed at $2\theta = 19.8^\circ$, even for a wide diffraction angle of $2\theta = 10\text{--}60^\circ$ (Figure S1). The peak at 19.8° was assigned to P(VDF-TrFE) (110)/(200), with a crystalline β -phase (JCPDS Card No. 38-1638). This implies that all P(VDF-TrFE) specimens have both ferroelectricity and piezoelectricity [24]. The full width at half maximum (FWHM) of the peak varies, depending on the spin coating conditions. Specifically, the FWHM continuously decreases with increasing distance. However, the FWHM initially decreases and then increases with increasing rotational speed. This result implies that the grain size of β -phase P(VDF-TrFE) increases with increasing distance, while the grain size initially increases and then decreases with increasing rotational speeds.

Figure 1d shows the atomic force microscopy (AFM) images (1×1 μm^2) of P(VDF-TrFE) film specimens. The surface morphology of all specimens is rather similar, displaying submicron-sized hills and pits. All surfaces are quite flat with a small root-mean-square roughness of $R_{\text{rms}} = 7.0\text{--}7.8$ nm, regardless of distance and rotational speed.

The distance from the center during spin coating affected the electrical, mechanical, and microstructure properties of the P(VDF-TrFE) films. Figure 2a shows the polarization–electric field loops of the P(VDF-TrFE) films fabricated at various distances from the center. Note that the rotational speed was kept constant at $\omega = 3000$ rpm. Irrespective of the distance, all of the P(VDF-TrFE) films clearly showed hysteresis loops, confirming their ferroelectric properties. The remnant polarization of the films slightly increased with increasing distance, for example, from 5.62 $\mu\text{C}/\text{cm}^2$ at $r = 0$ cm to 6.63 $\mu\text{C}/\text{cm}^2$ at $r = 4$ cm, while the coercive field remained almost unchanged (0.58 MV/cm). The same trend was observed in the complex dielectric constant (Figure 2b), with the dielectric constant at 1 kHz increasing with increasing distance (e.g., from 12.95 at $r = 0$ cm to 13.85 at $r = 4$ cm), and

the dielectric loss $\tan\delta$ remained almost constant (0.047) over a wide frequency range of $f = 10^2$ – 10^6 Hz.

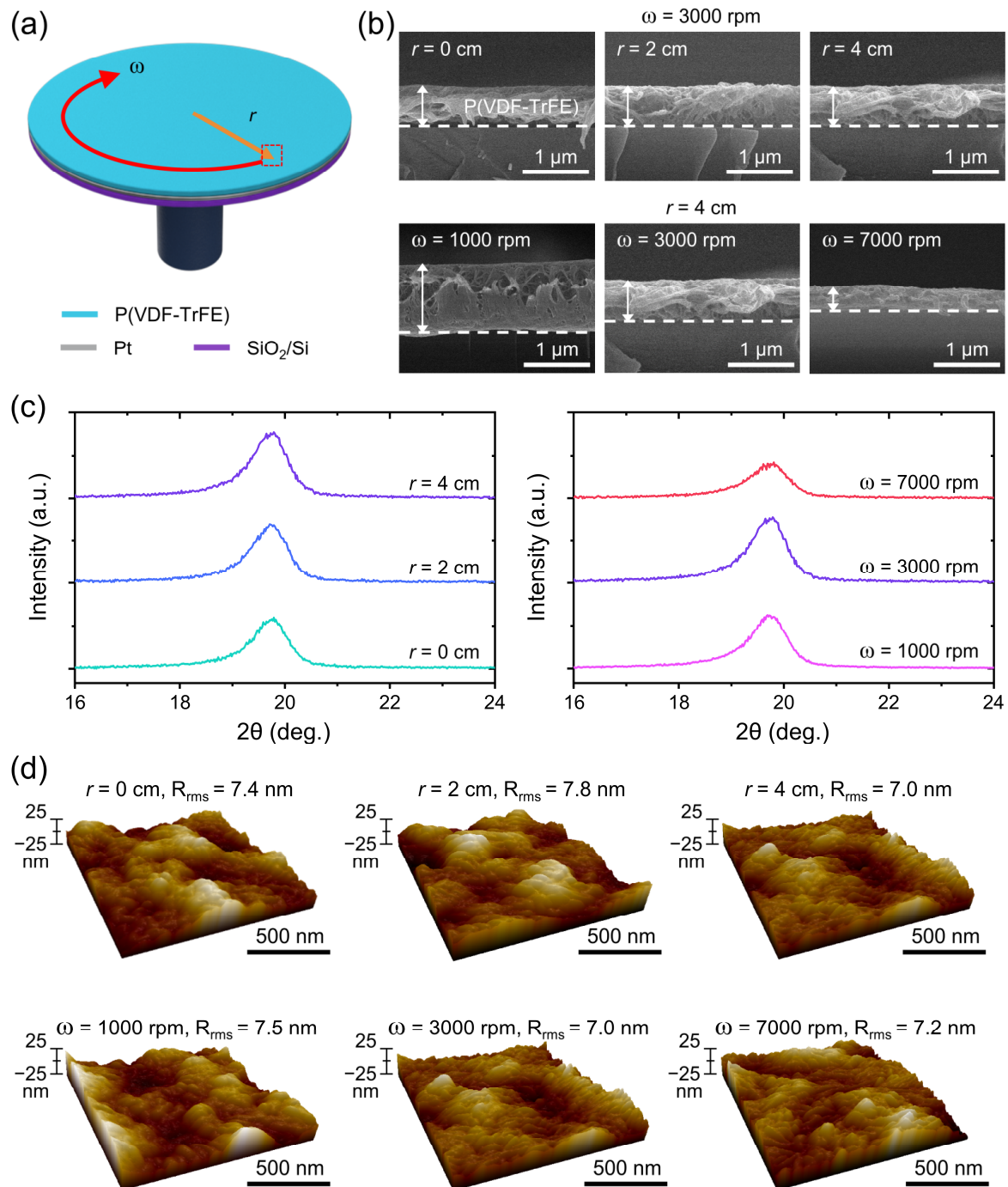


Figure 1. (a) Schematic of the spin coating of P(VDF-TrFE) films on a Pt-coated SiO₂/Si substrate. Film specimens were taken at various distances (r) from the center and under different rotational speeds (ω). (b) Cross-sectional scanning electron microscopy (SEM) images of P(VDF-TrFE) films. The interface between film and substrate is denoted by dashed lines. (c) X-ray diffraction patterns and (d) atomic force microscopy (AFM) images of spin-coated P(VDF-TrFE) film specimens obtained at various distances from the center and under different rotational speeds. In (d), the root-mean-square value of roughness (R_{rms}) is shown for each image.

Figure 2c,d show the differential scanning calorimetry (DSC) heating thermogram and crystallinity of P(VDF-TrFE), respectively. The sharp endothermic peak at $T_M = 150$ °C is

identified as the melting temperature [25]. Similar to previous reports [26,27], we estimated the crystallinity by comparing the melting enthalpy of a 100% crystalline film with that of the sample. The equation used to calculate the percentage crystallinity is expressed as follows:

$$X_c = \left(\frac{\Delta H_m}{\Delta H_m^0} \right) \times 100\% \quad (1)$$

where X_c is the percentage crystallinity of P(VDF-TrFE), ΔH_m is the melting enthalpy of the sample, and ΔH_m^0 is the melting enthalpy of a 100% crystalline P(VDF-TrFE) (91.45 mJ/mg) [28]. The results indicated that the crystallinities of the films fabricated at distances of $r = 0, 2,$ and 4 cm were estimated to be 32%, 33%, and 36%, respectively (Figure 2d). On the other hand, Young's modulus slightly increased with increasing distance, reaching values larger than 6 GPa at $r = 4$ cm (Figure 2e).

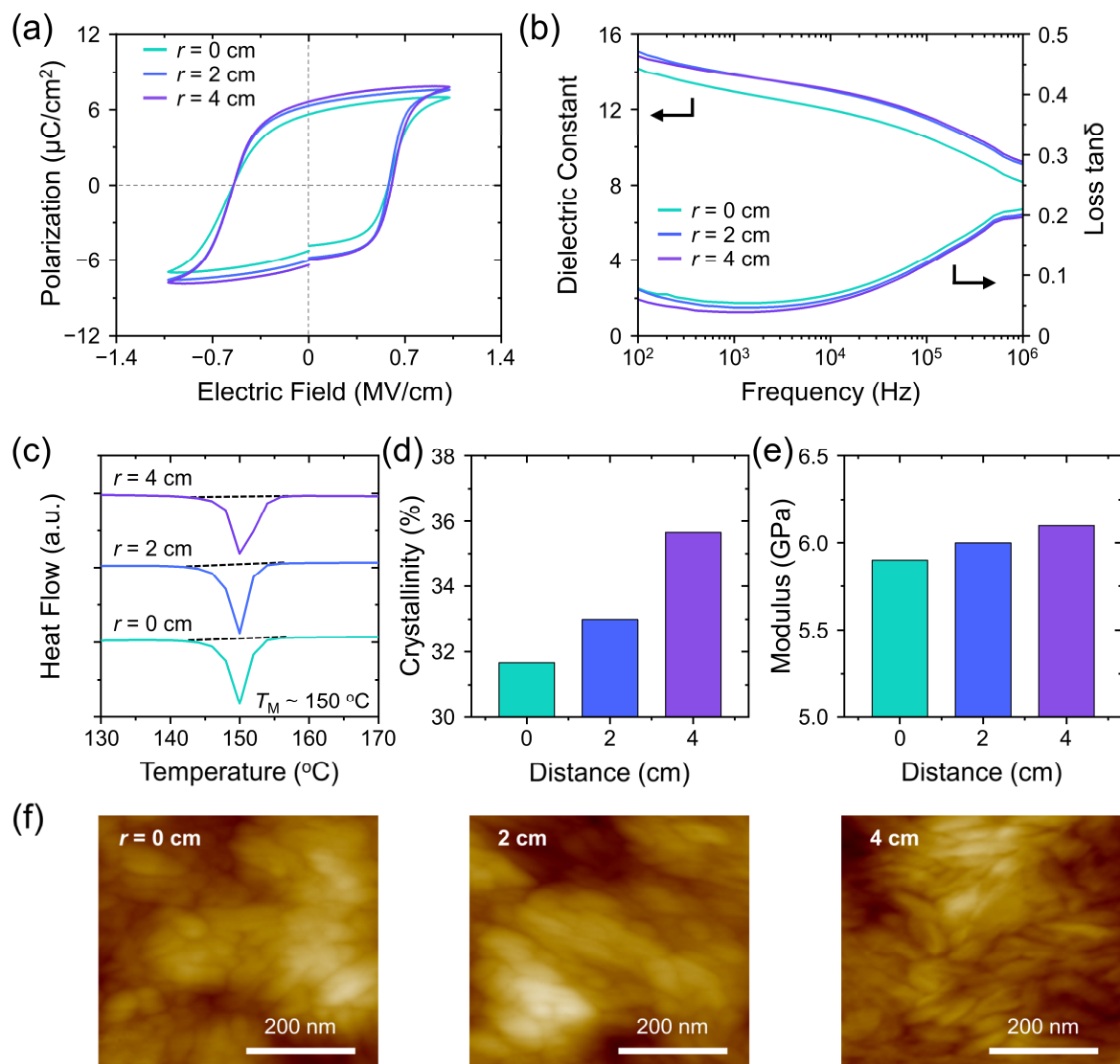


Figure 2. Distance-dependent (a) ferroelectric hysteresis loop, (b) dielectric constant and loss $\tan\delta$, (c) differential scanning calorimetry (DSC) heating thermogram, (d) crystallinity, (e) Young's modulus, and (f) surface morphology of P(VDF-TrFE) films. In (a–f), the rotational speed was fixed at $\omega = 3000$ rpm. In (c), the dashed lines represent the linear baselines for the enthalpy calculation. The T_M represents the melting temperature of P(VDF-TrFE).

The distance-dependent surface morphology of the P(VDF-TrFE) films is presented in Figure 2f. Atomic force microscopy (AFM) micrographs provided clear images of the

P(VDF-TrFE) grains. Although the surface roughness was similar (Figure 1d), the P(VDF-TrFE) film obtained at $r = 4$ cm had slightly longer and denser grains, compared with those at $r = 0$ and 2 cm. This increase in crystalline phase can be attributed to the enhanced centrifugal force at a larger distance, which spins off the amorphous phase in P(VDF-TrFE), as demonstrated in Figure 2d. In Table 1, we summarize the electrical, dielectric, and mechanical properties of the P(VDF-TrFE) film specimens obtained at various distances under $\omega = 3000$ rpm.

Table 1. Distance-dependent physical properties of P(VDF-TrFE) films during the spin coating. The rotational speed was fixed at 3000 rpm.

Distance	Thickness	Roughness	Remnant Polarization	Dielectric Constant at 1 kHz	Dielectric Loss at 1 kHz	Crystallinity	Young's Modulus
0 cm	632 nm	7.4 nm	5.62 $\mu\text{C}/\text{cm}^2$	12.95	0.055	31.67%	5.9 GPa
2 cm	620 nm	7.8 nm	6.30 $\mu\text{C}/\text{cm}^2$	13.82	0.047	32.99%	6.0 GPa
4 cm	640 nm	7.0 nm	6.63 $\mu\text{C}/\text{cm}^2$	13.85	0.039	35.66%	6.1 GPa

The rotational speed during spin coating strongly affected the electrical, mechanical, and microstructure properties of the P(VDF-TrFE) films. Notably, the remnant polarization (Figure 3a), complex dielectric constant (Figure 3b), and crystallinity (Figure 3c,d) showed an increase, with increasing rotational speed from 1000 rpm to 3000 rpm, but a decrease at 7000 rpm. As an example, the remnant polarizations were estimated to be 6.23, 6.63, and 5.34 $\mu\text{C}/\text{cm}^2$ for $\omega = 1000, 3000,$ and 7000 rpm, respectively. Note that the distance from the center was maintained at $r = 4$ cm.

In contrast, Young's modulus continuously increased with increasing rotational speed and reached 9 GPa at $\omega = 7000$ rpm (Figure 3e). This three-fold enhancement of a thin (~ 360 nm) P(VDF-TrFE) film, compared to the Young's modulus of ~ 3 GPa for thick (>50 μm) P(VDF-TrFE) films, is unusual [29]. Similar enhancements of the Young's modulus at reduced thickness have been reported in the rubbery states of several polymers, above the glass transition temperature [30–32]. Although the mechanism is yet to be clarified, it is believed that nanoconfinement is expected to modify the intermolecular interactions in P(VDF-TrFE), thereby enhancing the Young's modulus [30].

Rotational speed-dependent surface morphologies are presented in Figure 3f. Although the surface roughness was similar (Figure 1d), the grains of the P(VDF-TrFE) films became more compact and elongated with increasing rotational speed. These observations are consistent with an increased mechanical stretching and alignment of the polymeric chain due to increasing shear stress [33]. In Table 2, we summarize the electrical, dielectric, and mechanical properties of the P(VDF-TrFE) film specimens obtained under various rotational speeds at $r = 4$ cm.

Table 2. Rotational speed-dependent physical properties of P(VDF-TrFE) films during the spin coating. The distance from the center was fixed at 4 cm.

Rotation Speed	Thickness	Roughness	Remnant Polarization	Dielectric Constant at 1 kHz	Dielectric Loss at 1 kHz	Crystallinity	Young's Modulus
1000 rpm	1080 nm	7.5 nm	6.23 $\mu\text{C}/\text{cm}^2$	13.42	0.040	33.91%	5.8 GPa
3000 rpm	640 nm	7.0 nm	6.63 $\mu\text{C}/\text{cm}^2$	13.85	0.039	35.66%	6.1 GPa
7000 rpm	360 nm	7.2 nm	5.34 $\mu\text{C}/\text{cm}^2$	11.97	0.033	31.50%	8.9 GPa

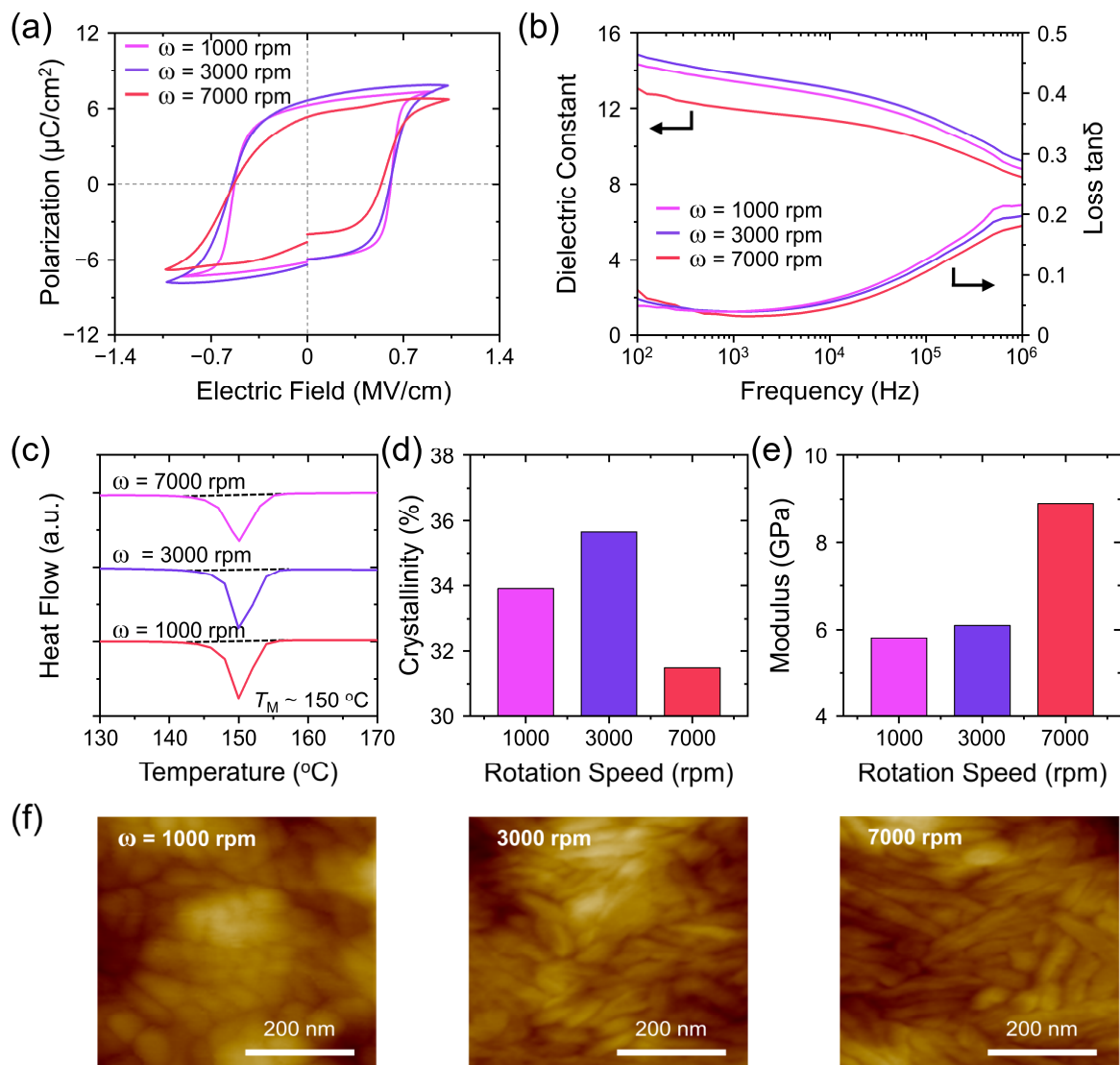


Figure 3. Rotational speed-dependent (a) ferroelectric hysteresis loop, (b) dielectric constant and loss $\tan\delta$, (c) differential scanning calorimetry (DSC) heating thermogram, (d) crystallinity, (e) Young's modulus, and (f) surface morphology of P(VDF-TrFE) films. In (a–f), the distance was fixed at $r = 4$ cm. In (c), the dashed lines represent the linear baselines for the enthalpy calculation. The T_M represents the melting temperature of P(VDF-TrFE).

To elucidate the variation of physical properties of spin-coated P(VDF-TrFE) films in detail, we show the Fourier transform infrared (FT-IR) absorbance spectra in Figure 4a,b. Note that we did not normalize the data, but removed the background. The absorption spectra were observed to be significantly affected by the increasing rotational speed, rather than the distance. In particular, the absorption peaks originating from the CF₂ stretching modes at 843 cm⁻¹ and 1282 cm⁻¹, and the CH₂ wagging vibration mode at 1076 cm⁻¹, which correspond to the crystalline β -phase, significantly decreased with increasing rotational speed [34]. On the other hand, the absorption peak originating from the CF₂ rocking mode at 763 cm⁻¹, which corresponds to the crystalline α -phase, slightly decreased [35]. Such variations are not obvious for distance-dependence.

The content of the crystalline phase of P(VDF-TrFE) was quantified using FT-IR absorbance spectra. In accordance with previous studies [36,37], the relative fraction of the β -crystalline phase was obtained using the following formula:

$$F(\beta) = \frac{A_{\beta}}{(K_{\beta}/K_{\alpha})A_{\alpha} + A_{\beta}} \quad (2)$$

where $F(\beta)$ represents the fraction of the β -crystalline phase, and A_{α} and A_{β} denote the absorbance at 763 cm^{-1} and 843 cm^{-1} , respectively, in arbitrary units. K_{α} and K_{β} correspond to the absorption coefficient at the respective wavenumbers, recorded as $6.1 \times 10^4 \text{ cm}^2/\text{mol}$ and $7.7 \times 10^4 \text{ cm}^2/\text{mol}$, respectively. As shown in Figure 4a, the fraction of the β -crystalline phase in spin-coated P(VDF-TrFE) films continuously increases with increasing distance from the center. On the other hand, the fraction of the β -crystalline phase initially increases and then decreases with increasing rotational speed (Figure 4b), similar to the results in Figures 2 and 3.

Considering the paraelectricity of the α -crystalline phase of P(VDF-TrFE) [24], the decreased remnant polarization and dielectric constant at $\omega = 7000 \text{ rpm}$ should be consistent with the sharply decreased fraction of the β -crystalline phase. Considering the lower angle of the Bragg diffraction peak of α -phase ($2\theta = 18.5^\circ$) than that of β -phase ($2\theta = 19.8^\circ$) of P(VDF-TrFE) [24], the broad X-ray diffraction peak at $\omega = 7000 \text{ rpm}$ should also be consistent with the sharply decreased fraction of β -crystalline phase (i.e., increased fraction of α -crystalline phase). While more investigation is highly required, the sharply decreased fraction of the β -crystalline phase at a higher rotation speed might be originated from the reduced thickness-induced weak crystallization of the piezoelectric β -phase in the P(VDF-TrFE) films, as discussed in Ref. [38].

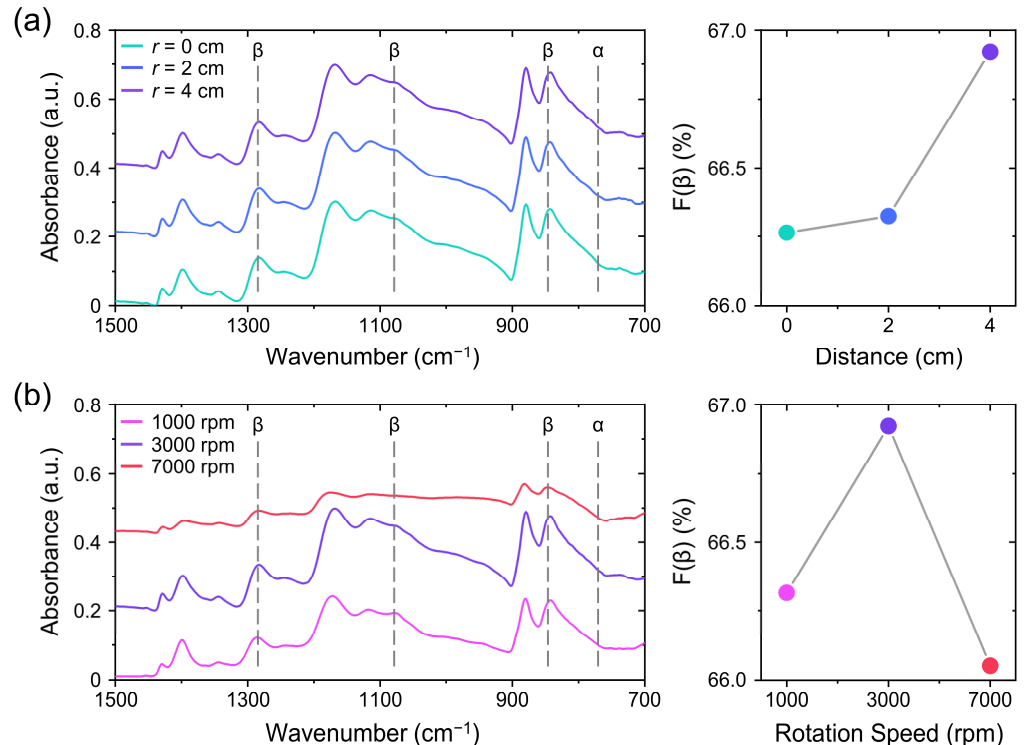


Figure 4. Fourier transform-infrared (FT-IR) absorbance spectra and the relative fraction of piezoelectric β -crystalline phase of spin-coated P(VDF-TrFE) film specimens obtained (a) at various distances from the center and (b) under different rotational speeds. In (a,b), characteristic absorbance bands were labeled for the α - and β -phases.

After characterizing the structural, electrical, mechanical, and microstructural properties of the P(VDF-TrFE) film specimens as a function of distance and rotational speed, we investigated the piezoelectric power generation performance of a P(VDF-TrFE)-based piezoelectric nanogenerator (PENG). Figure 5a shows the schematic diagram and a digital photograph of the PENG. Notably, we deposited a thin layer of PMMA polymer to protect the P(VDF-TrFE) film from mechanical shock during the periodic cycles of pressing and releasing. During the press, a piezoelectric potential developed across the film, and free charges developed on the metal electrodes to screen the potential, which resulted in a flow of charge carriers. Conversely, when the P(VDF-TrFE) was released, the induced piezoelectric potential was diminished, which resulted in a reverse flow of charge carriers (Figure 5b). As a result, two alternating current peaks occurred during each cycle of pressing and releasing.

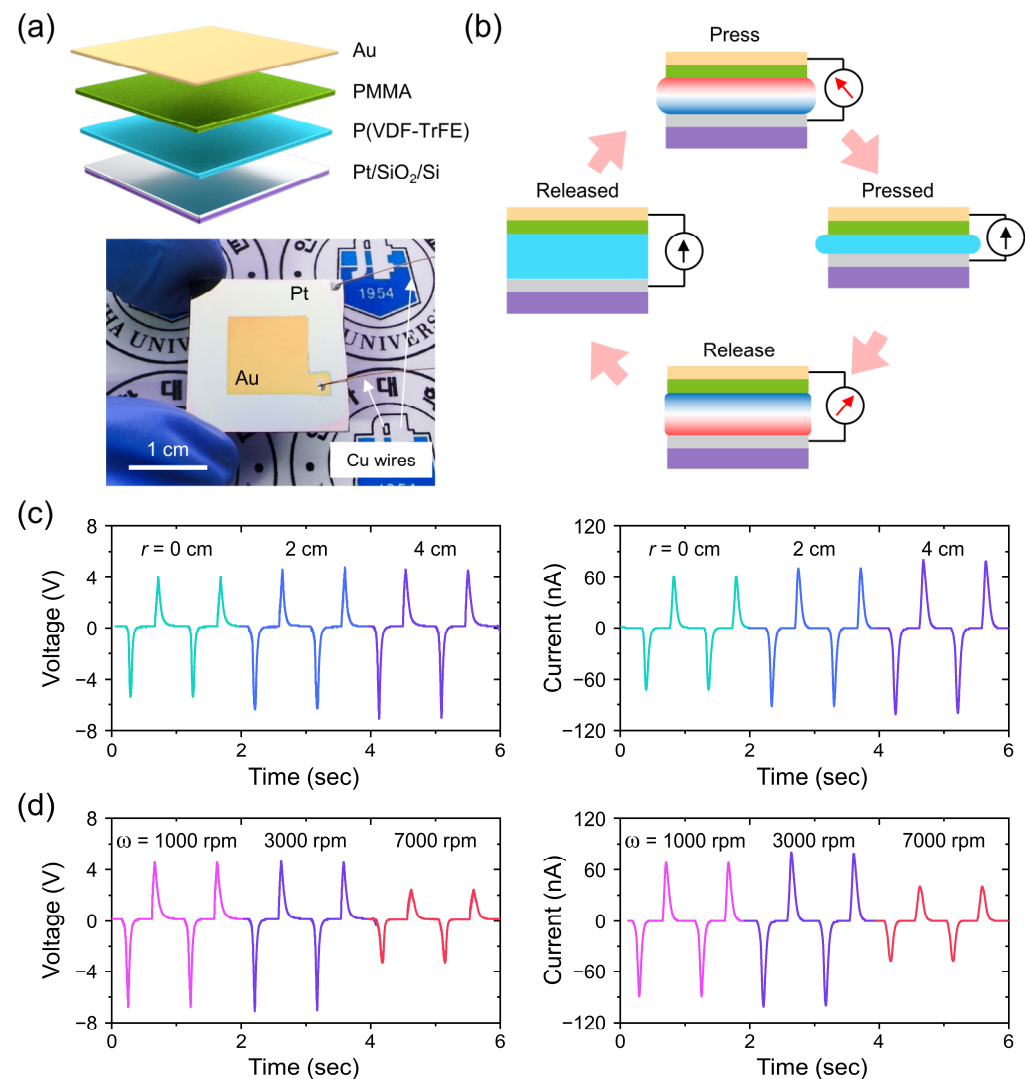


Figure 5. (a) Schematic diagram and a digital image, and (b) power generation mechanism of a P(VDF-TrFE)-based piezoelectric nanogenerator (PENG) during one cycle of the pressing and releasing process. (c) Distance- and (d) rotational speed-dependent open-circuit voltage and short-circuit current. In (a), two Cu wires were attached to Au as a top electrode and Pt as a bottom electrode. In (b), the gradient red-white-blue color represents the piezoelectric potential, induced during press and release of P(VDF-TrFE) film.

Figure 5c,d show the distance- and rotational speed-dependent piezoelectric outputs, respectively. The open-circuit voltage and short-circuit current continuously increase with

increasing distance. On the other hand, the open-circuit voltage and short-circuit current initially increase and then decrease with increasing rotational speed. The peak-to-peak voltage and current were maximized at $r = 4$ cm, at which the remnant polarization was also maximized. Additionally, the peak-to-peak voltage and current were minimized at $\omega = 7000$ rpm, at which Young's modulus was maximized.

In Table 3, we compared the obtained piezoelectric outputs with the remnant polarization and Young's modulus of the P(VDF-TrFE) film specimens obtained at various distances under different rotational speeds. The piezoelectric output is proportional to the remnant polarization divided by the Young's modulus for all specimens. Considering that the piezoelectric coefficient is proportional to the remnant polarization and inversely proportional to the Young's modulus [39], the observed voltage and current behaviors indicate the significance of the piezoelectric coefficient to the piezoelectric output [40].

Table 3. A comparison of piezoelectric output with the remnant polarization over Young's modulus for P(VDF-TrFE) films obtained at various distances under different rotational speeds.

Specimen		Peak-to-Peak Voltage	Peak-to-Peak Current	Polarization/Modulus
1000 rpm	4 cm	11.34 V	155.89 nA	$1.07 \mu\text{C}/\text{cm}^2 \cdot \text{GPa}^{-1}$
	0 cm	9.49 V	134.27 nA	$0.95 \mu\text{C}/\text{cm}^2 \cdot \text{GPa}^{-1}$
3000 rpm	2 cm	11.02 V	162.73 nA	$1.05 \mu\text{C}/\text{cm}^2 \cdot \text{GPa}^{-1}$
	4 cm	11.74 V	181.71 nA	$1.09 \mu\text{C}/\text{cm}^2 \cdot \text{GPa}^{-1}$
7000 rpm	4 cm	5.75 V	87.64 nA	$0.60 \mu\text{C}/\text{cm}^2 \cdot \text{GPa}^{-1}$

To date, there have been several reports for enhancing the piezoelectric coefficient of thick P(VDF-TrFE) films, including electrospinning [41], nanoimprint lithography [42], and mechanical shearing/drawing [43]. However, there are limited options for thin P(VDF-TrFE) films, apart from the use of local pressure with a nanoscale tip of scanning probe microscopy [16].

As demonstrated in Figures 2–4, the piezoelectric properties of thin P(VDF-TrFE) films can also be modified through a simple spin coating process. The centrifugal force-induced shear stress can affect the crystallinity of the materials and the degree of alignment of the dipoles, which is linked to the local polarization. Centrifugal force can also modify the Young's modulus through thickness-induced confinement. Moreover, the reduced thickness can degrade the piezoelectric properties. The degradation of piezoelectricity in thin P(VDF-TrFE) is likely due to increased strain and orientation mismatches between neighboring crystallines, leading to the formation of large amorphous regions, as discussed in Ref. [38]. Therefore, careful optimization of the spin coating condition is necessary for the efficient P(VDF-TrFE)-based piezoelectric nanogenerators, as the piezoelectric output power is significantly influenced by the piezoelectricity.

In addition to optimizing spin coating conditions, other options to consider include the use of solvents with higher dipole moments, such as dimethyl sulfoxide (DMSO) instead of DMF [44], optimizing the annealing temperature slightly above the Curie temperature [45], and adding particulate or fibrous filler [46] during the synthesis of thin P(VDF-TrFE) films with enhanced piezoelectricity.

4. Summary

In conclusion, we systematically investigated the effects of distance and rotational speed on the structural, electrical, mechanical, and microstructural properties of spin-coated P(VDF-TrFE) films. The distance from the center varied from 0 to 4 cm, and the rotation speed was set from 1000 to 7000 rpm. All P(VDF-TrFE) film specimens displayed ferroelectricity and piezoelectricity. The remnant polarization, dielectric constant, and crystallinity increased with increasing distance from the center, while the film thickness and Young's modulus remained constant. On the other hand, the remnant polarization, dielectric constant, and crystallinity initially increased and then decreased with increasing

rotational speed, while the film thickness decreased and the Young's modulus increased continuously. Fourier transform-infrared absorbance spectra indicated that the crystalline β -phase continuously increased with increasing distance, but initially increased and then decreased with increasing rotational speed. The piezoelectric power outputs of the P(VDF-TrFE)-based piezoelectric nanogenerator were dependent on the spin coating condition. The specimen with the maximum remnant polarization had the largest piezoelectric current (181.71 nA), while the specimen with the maximum Young's modulus had the smallest (87.64 nA). These behaviors were explained by centrifugal force-induced shear stress and grain alignment, as well as thickness-dependent β -phase crystallization and confinement effects. To achieve enhanced piezoelectric output from spin-coated P(VDF-TrFE) films, the fine optimization of distance and rotational speed is crucial, as the piezoelectric properties are strongly dependent on the remnant polarization, the Young's modulus, and the fraction of crystalline β -phase.

Supplementary Materials: The following supporting information can be downloaded at: <https://www.mdpi.com/article/10.3390/en16041892/s1>, Figure S1: X-ray diffraction patterns of spin-coated P(VDF-TrFE) film specimens obtained at various distances from the center and rotational speeds for a wide diffraction angle of $2\theta = 10\text{--}60^\circ$.

Author Contributions: Conceptualization, J.H.J. and D.G.J.; investigation and data curation, D.G.J., H.H.S. and M.S.K.; writing—original draft preparation, J.H.J. and D.G.J.; writing—review and editing, J.H.J., D.G.J. and H.H.S. All authors have read and agreed to the published version of the manuscript.

Funding: This work was supported by Inha University Research Grant.

Conflicts of Interest: The authors declare no conflict of interest.

References

1. Wang, Z.L.; Wu, W. Nanotechnology-enabled energy harvesting for self-powered micro-/nanosystems. *Angew. Chem. Int. Ed.* **2012**, *51*, 11700–11721. [[CrossRef](#)] [[PubMed](#)]
2. Wang, Z.L. Triboelectric nanogenerators as new energy technology for self-powered systems and as active mechanical and chemical sensors. *ACS Nano* **2013**, *7*, 9533–9557. [[CrossRef](#)] [[PubMed](#)]
3. Boyle, G. *Renewable Energy: Power for a Sustainable Future*, 3rd ed.; Oxford University Press: Oxford, UK, 2012.
4. Wang, Z.L.; Song, J.H. Piezoelectric nanogenerators based on zinc oxide nanowire arrays. *Science* **2006**, *312*, 242–246. [[CrossRef](#)]
5. Jin, D.W.; Ko, Y.J.; Ahn, C.W.; Hur, S.; Lee, T.K.; Jeong, D.G.; Lee, M.; Kang, C.-Y.; Jung, J.H. Polarization- and electrode-optimized polyvinylidene fluoride films for harsh-environmental piezoelectric nanogenerator applications. *Small* **2021**, *17*, 2007289. [[CrossRef](#)] [[PubMed](#)]
6. Naqvi, A.; Ali, A.; Altabey, W.A.; Kouritem, S.A. Energy harvesting from fluid flow using piezoelectric materials: A Review. *Energies* **2022**, *15*, 7424. [[CrossRef](#)]
7. Sahu, M.; Hajra, S.; Lee, K.; Deepti, P.L.; Mistewicz, K.; Kim, H.J. Piezoelectric nanogenerator based on lead-free flexible PVDF-barium titanate composite films for driving low power electronics. *Crystals* **2021**, *11*, 85. [[CrossRef](#)]
8. Yang, Z.; Zhou, S.; Zu, J.; Inman, D. High-performance piezoelectric energy harvesters and their applications. *Joule* **2018**, *2*, 642–697. [[CrossRef](#)]
9. Jung, J.H.; Lee, M.; Hong, J.-I.; Ding, Y.; Chen, C.-Y.; Chou, L.-J.; Wang, Z.L. Lead-free NaNbO_3 nanowires for a high output piezoelectric nanogenerator. *ACS Nano* **2011**, *12*, 10041–10046. [[CrossRef](#)]
10. Koka, A.; Sodano, H.A. High-sensitivity accelerometer composed of ultra-long vertically aligned barium titanate nanowire arrays. *Nat. Commun.* **2013**, *4*, 2682. [[CrossRef](#)]
11. Zhao, X.J.; Zhu, G.; Wang, Z.L. Coplanar induction enabled by asymmetric permittivity of dielectric materials for mechanical energy conversion. *ACS Appl. Mater. Interfaces* **2015**, *7*, 6025–6029. [[CrossRef](#)]
12. Kwon, J.; Seung, W.; Sharma, B.K.; Kim, S.-W.; Ahn, J.-H. A high performance PZT ribbon-based nanogenerator using graphene transparent electrodes. *Energy Environ. Sci.* **2012**, *5*, 8970–8975. [[CrossRef](#)]
13. Zhang, Q.M.; Bharti, V.; Zhao, X. Giant electrostriction and relaxor ferroelectric behavior in electron-irradiated Poly(vinylidene fluoride-trifluoroethylene) copolymer. *Science* **1998**, *280*, 2101–2104. [[CrossRef](#)] [[PubMed](#)]
14. Liu, Y.; Wang, Q. Ferroelectric polymers exhibiting negative longitudinal piezoelectric coefficient: Progress and prospects. *Adv. Sci.* **2020**, *7*, 1902468. [[CrossRef](#)] [[PubMed](#)]
15. Chu, B.; Zhou, X.; Ren, K.; Neese, B.; Lin, M.; Wang, Q.; Bauer, F.; Zhang, Q.M. A dielectric polymer with high electric energy density and fast discharge speed. *Science* **2006**, *313*, 334–336. [[CrossRef](#)] [[PubMed](#)]
16. Choi, Y.-Y.; Sharma, P.; Phatak, C.; Gosztola, D.; Liu, Y.; Lee, J.; Lee, B.; Li, J.; Gruverman, A.; Ducharme, S.; et al. Enhancement of local piezoresponse in polymer ferroelectrics via nanoscale control of microstructure. *ACS Nano* **2015**, *9*, 1809–1819. [[CrossRef](#)]

17. Yang, J.H.; Ryu, T.; Lansac, Y.; Jang, Y.H.; Lee, B.H. Shear stress-induced enhancement of the piezoelectric properties of PVDF-TrFE thin films. *Org. Electron.* **2016**, *28*, 67–72. [[CrossRef](#)]
18. Sahu, N.; Parija, B.; Panigrahi, S. Fundamental understanding and modeling of spin coating process: A review. *Indian J. Phys.* **2009**, *83*, 493–502. [[CrossRef](#)]
19. Fortunato, M.; Cavallini, D.; Bellis, G.D.; Marra, F.; Tamburrano, A.; Sarto, F.; Sarto, M.S. Phase inversion in PVDF films with enhanced piezoresponse through spin-coating and quenching. *Polymers* **2019**, *11*, 1096. [[CrossRef](#)]
20. Wang, H.; Chen, L.; Xing, R.; Liu, J.; Han, Y. Simultaneous control over both molecular order and long-range alignment in films of the donor–acceptor copolymer. *Langmuir* **2015**, *31*, 469–479. [[CrossRef](#)]
21. Furukawa, T. Ferroelectric properties of vinylidene fluoride copolymers. *Phase Transit.* **1989**, *18*, 143–211. [[CrossRef](#)]
22. Jung, J.H.; Chen, C.-Y.; Yun, B.K.; Lee, N.; Zhou, Y.; Jo, W.; Chou, L.-J.; Wang, Z.L. Lead-free KNbO₃ ferroelectric nanorod based flexible nanogenerators and capacitors. *Nanotechnology* **2012**, *23*, 375401. [[CrossRef](#)] [[PubMed](#)]
23. Chan, J.M.; Wang, M. Visualizing the orientation of single polymers induced by spin-coating. *Nano Lett.* **2022**, *22*, 5891–5897. [[CrossRef](#)] [[PubMed](#)]
24. Bellet-Amalric, E.; Legrand, J.F. Crystalline structures and phase transition of the ferroelectric P(VDF-TrFE) copolymers, A Neutron Diffraction Study. *Eur. Phys. J. B* **1998**, *3*, 225–236. [[CrossRef](#)]
25. Gregorio, R., Jr.; Botta, M.M. Effect of crystallization temperature on the phase transitions of P(VDF-TrFE) copolymers. *J. Polym. Sci. B: Polym. Phys.* **1998**, *36*, 403–414. [[CrossRef](#)]
26. Ma, W.; Zhang, J.; Wang, X.; Wang, S. Effect of PMMA on crystallization behavior and hydrophilicity of poly(vinylidene fluoride)/poly(methyl methacrylate) blend prepared in semi-dilute solutions. *Appl. Surf. Sci.* **2007**, *253*, 8377–8388. [[CrossRef](#)]
27. Jeong, D.G.; Ko, Y.J.; Kim, J.H.; Kong, D.S.; Hu, Y.C.; Lee, D.W.; Im, S.H.; Lee, J.; Kim, M.S.; Lee, G.-H.; et al. On the origin of enhanced power output in ferroelectric polymer-based triboelectric nanogenerators: Role of dipole charge versus piezoelectric charge. *Nano Energy* **2022**, *103*, 107806. [[CrossRef](#)]
28. Lonjon, A.; Laffont, L.; Dumont, P.; Dantras, E.; Lacabanne, C. Structural and electrical properties of gold nanowires/P(VDF-TrFE) nanocomposites. *J. Phys. D Appl. Phys.* **2010**, *43*, 345401. [[CrossRef](#)]
29. Hahm, S.-W.; Khang, D.-Y. Crystallization and microstructure-dependent elastic moduli of ferroelectric P(VDF-TrFE) thin films. *Soft Matter* **2010**, *6*, 5802–5806. [[CrossRef](#)]
30. Nguyen, H.K.; Fujinami, S.; Nakajima, K. Size-dependent elastic modulus of ultrathin polymer films in glassy and rubbery states. *Polymer* **2016**, *105*, 64–71. [[CrossRef](#)]
31. Saito, M.; Ito, K.; Yokoyama, H. Mechanical properties of ultrathin polystyrene-b-polybutadiene-b-polystyrene block copolymer films: Film thickness-dependent young's modulus. *Macromolecules* **2021**, *54*, 8538–8547. [[CrossRef](#)]
32. Wang, J.; Shi, F.G.; Nieh, T.G.; Zhao, B.; Brongo, M.R.; Qu, S.; Rosenmayer, T. Thickness dependence of elastic modulus and hardness of on-wafer low-k ultrathin polytetrafluoroethylene films. *Scripta Mater.* **2000**, *42*, 687–694. [[CrossRef](#)]
33. Jung, H.J.; Chang, J.; Park, Y.J.; Kang, S.J.; Lotz, B.; Huh, J.; Park, C. Shear-induced ordering of ferroelectric crystals in spin-coated thin poly(vinylidene fluoride-co-trifluoroethylene) films. *Macromolecules* **2009**, *42*, 4148–4154. [[CrossRef](#)]
34. Arrigoni, A.; Brambilla, L.; Bertarelli, C.; Serra, G.; Tommasini, M.; Castiglioni, C. P(VDF-TrFE) nanofibers: Structure of the ferroelectric and paraelectric phases through IR and raman spectroscopies. *RSC Adv.* **2020**, *10*, 37779–37796. [[CrossRef](#)]
35. Arshad, A.N.; Wahid, M.H.M.; Rusop, M.; Majid, W.H.A.; Subban, R.H.Y.; Rozana, M.D. Dielectric and structural properties of poly(vinylidene fluoride) (PVDF) and poly(vinylidene fluoride-trifluoroethylene) (PVDF-TrFE) filled with magnesium oxide nanofillers. *J. Nanomater.* **2019**, *2019*, 5961563. [[CrossRef](#)]
36. Suresh, G.; Mallikarjunachari, G.; Jatav, S.; Thirmal, C.; Rao, M.S.R.; Satapathy, D.K. Evolution of morphology, ferroelectric, and mechanical properties in poly(vinylidene fluoride)-poly(vinylidene fluoride-trifluoroethylene) blends. *J. Appl. Polym. Sci.* **2018**, *135*, 45955. [[CrossRef](#)]
37. Haque, R.I.; Vié, R.; Germainy, M.; Valbin, L.; Benaben, P.; Boddaert, X. Inkjet printing of high molecular weight PVDF-TrFE for flexible electronics. *Flex. Print. Electron.* **2016**, *1*, 015001. [[CrossRef](#)]
38. Zhang, Q.M.; Xu, H.; Fang, F.; Cheng, Z.-Y.; Xia, F.; You, H. Critical thickness of crystallization and discontinuous change in ferroelectric behavior with thickness in ferroelectric polymer thin films. *J. Appl. Phys.* **2001**, *89*, 2613–2616. [[CrossRef](#)]
39. Broadhurst, M.G.; Davis, G.T. Physical basis for piezoelectricity in PVDF. *Ferroelectrics* **1984**, *60*, 3–13. [[CrossRef](#)]
40. Jaffe, B.; Cook, W.R., Jr.; Jaffe, H. *Piezoelectric Ceramics*; Academic Press: London, UK, 1971.
41. Andrew, J.S.; Clarke, D.R. Effect of electrospinning on the ferroelectric phase content of polyvinylidene difluoride fibers. *Langmuir* **2008**, *24*, 670–672. [[CrossRef](#)]
42. Hu, Z.J.; Tian, M.W.; Nysten, B.; Jonas, A.M. Regular arrays of highly ordered ferroelectric polymer nanostructures for non-volatile low-voltage memories. *Nat. Mater.* **2009**, *8*, 62–67. [[CrossRef](#)]
43. Chang, J.; Jung, H.J.; Jeong, H.; Park, Y.J.; Sung, J.; Kang, S.J.; Jung, G.Y.; Sung, M.M.; Park, C. One-step micropatterning of highly-ordered semi-crystalline poly(vinylidene fluoride-co-trifluoroethylene) films by a selective shear and detachment process. *Org. Electron.* **2011**, *12*, 98–107. [[CrossRef](#)]
44. Kim, J.; Lee, J.H.; Ryu, H.; Lee, J.-H.; Khan, U.; Kim, H.; Kwak, S.S.; Kim, S.-W. High-performance piezoelectric, pyroelectric, and triboelectric nanogenerators based on P(VDF-TrFE) with controlled crystallinity and dipole alignment. *Adv. Funct. Mater.* **2017**, *27*, 1700702. [[CrossRef](#)]

45. Mahdi, R.I.; Gan, W.C.; Majid, W.H.A. Hot plate annealing at a low temperature of a thin ferroelectric P(VDF-TrFE) film with an improved crystalline structure for sensors and actuators. *Sensors* **2014**, *14*, 19115–19127. [[CrossRef](#)] [[PubMed](#)]
46. Poudel, A.; Fernandez, M.A.; Tofail, S.A.M.; Biggs, M.J.P. Boron nitride nanotube addition enhances the crystallinity and cytocompatibility of PVDF-TrFE. *Front. Chem.* **2019**, *7*, 364. [[CrossRef](#)] [[PubMed](#)]

Disclaimer/Publisher’s Note: The statements, opinions and data contained in all publications are solely those of the individual author(s) and contributor(s) and not of MDPI and/or the editor(s). MDPI and/or the editor(s) disclaim responsibility for any injury to people or property resulting from any ideas, methods, instructions or products referred to in the content.